INTERNATIONAL JOURNAL FOR NUMERICAL METHODS IN FLUIDS
Int. J. Numer. Meth. Fluids 2004; **44**:957–973 (DOI: 10.1002/fld.677)

Development of an adaptive discontinuity-capturing hyperbolic finite element model

C. C. Fang and Tony W. H. Sheu*,†

Department of Engineering Science and Ocean Engineering, National Taiwan University, 73 Chow-Shan Road, Taipei, Taiwan, Republic of China

SUMMARY

In this paper we present a five-parameter Taylor–Galerkin finite element model to simulate Euler equations in a domain of two dimensions. The introduced free parameters are theoretically determined by employing M-matrix theory to obtain a physically correct and non-oscillatory solution in regions containing a sharp solution profile. To improve the computational efficiency and solution accuracy, grids are adaptively added to obtain solutions with fewer mesh points. The discontinuity-capturing finite element model has been validated against test cases, reproducing analytical solutions to the gas dynamic problems under the current investigation. Copyright © 2004 John Wiley & Sons, Ltd.

KEY WORDS: Taylor–Galerkin; Euler equations; M-matrix theory; monotonicity; adaptively; discontinuity capturing

1. INTRODUCTION

We employ in this study the finite element method to simulate the hyperbolic-type gas dynamic equations due to its ability to tackle complex geometry problem and to accurately implement Neumann-type boundary condition. In the literature, several characteristic-type finite element methods are often referred to, among which are the characteristic finite element method [1], discontinuous finite element method [2], and the characteristic Galerkin finite element method [3]. For an extensive survey of these methods, one can refer to Donea [4]. The Petrov–Galerkin models [5, 6] have also gained widespread acceptance. This class of models was developed by introducing the upwinding mechanism into the weak statement. We will restrict ourselves to the Taylor–Galerkin finite element model [7].

*Correspondence to: Tony W. H. Sheu, Department of Engineering Science and Ocean Engineering, National Taiwan University, 73 Chow-Shan Road, Taipei, Taiwan, Republic of China.
†E-mail: twhsheu@ntu.edu.tw.

Contract/grant sponsor: National Science Council of the Republic of China; contract/grant number: NSC 88-2611-E-002-025

Received 24 February 2003
Revised 18 August 2003

As is well-known that an initially smooth solution to the gas dynamics equations may evolve to show a discontinuous distribution owing to the presence of non-linear terms in these equations [8]. To capture the sharply varying thermodynamic and field variables, the employed numerical methods should have the ability to resolve them within a fairly short distance. It is, therefore, essential to refine meshes in high-gradient regions and this need motivates the incorporation of adaptive grids into the present model development. In addition, the numerical method should give positive-valued and physically relevant oscillation-free Euler solutions. In this light, a model with the ability to yield monotonic solutions is also needed. Most of discontinuity-capturing schemes have, unfortunately, been theoretically justified in the one-dimensional case [9]. We therefore resort to the discontinuity-capturing model that has nothing to do with spatial dimensionality.

The remainder of this paper is organized as follows. Section 2 presents gas dynamic equations. In Section 3, we present some essential features of the five-parameter Taylor–Galerkin finite element model. These free parameters are rigorously determined so as to render a monotonicity-preserving finite element model. The guideline of ensuring scheme's monotonicity is the discrete maximum principle [10–13]. This is followed by determination of the diffusion coefficient introduced in Section 4, and some fundamental studies of the proposed model in Section 5. For efficiently resolving sharp profiles in the flow, we present the employed adaptive method [14] in Section 6. In Section 7, we present validation results in one dimension and then the simulated results for the two-dimensional shock reflection problem and the supersonic flow over a step. Finally, we draw conclusions in Section 8.

2. WORKING EQUATIONS

The Euler equations governing gas dynamics are expressed in conservation law form as

$$\mathbf{U}_t + \mathbf{F}_x + \mathbf{G}_y = 0 \tag{1}$$

where

$$\mathbf{U} = \begin{pmatrix} \rho \\ \rho u \\ \rho v \\ E \end{pmatrix} \tag{2}$$

In Equation (1), $\mathbf{F}$ and $\mathbf{G}$ are flux vectors along the x and y directions, respectively. These vectors are functions of the conservative field variable $\mathbf{U}$:

$$\mathbf{F} = \begin{pmatrix} \rho u \\ \rho u^2 + p \\ \rho uv \\ u(E + p) \end{pmatrix} \tag{3}$$

$$\mathbf{G} = \begin{pmatrix} \rho v \\ \rho uv \\ \rho v^2 + p \\ v(E + p) \end{pmatrix} \tag{4}$$

In the above, ρ, u, v, p and E are the density, x and y direction velocities, pressure and total energy, respectively. Note that shock and contact discontinuities, which, respectively, represent non-linear and linear degenerate fields [15], may co-exist in the Euler system of equations. To close the hyperbolic differential system, the chosen thermodynamic properties ρ, p, E are related by the following ideal gas equation of state:

$$p = (\bar{\gamma} - 1)(E - \tfrac{1}{2}\rho(u^2 + v^2)) \tag{5}$$

In the above, $\bar{\gamma}$ is the specific heat ratio.

3. NUMERICAL FORMULATION

In this paper, the Taylor–Galerkin finite element model will be developed for solving Equations (1)–(4). For easily describing the method, we will consider the following two-dimensional linear equation for ϕ in the flow field with a velocity vector (a, b):

$$\phi_t + f_x + g_y = 0 \tag{6}$$

where $f = a\phi$ and $g = b\phi$. We consider that both velocity components a and b in the x and y directions are constant.

Within the weighted residual framework, we introduce the weighting function $\mathbf{W}$ to obtain the finite element solution from the following integral equation:

$$\sum_{\mathrm{el}=1}^{n_{\mathrm{el}}} \int_{\Omega^{\mathrm{el}}} \int_{t_n}^{t_{n+1}} \mathbf{W}(x, y) \left[\frac{\partial \phi}{\partial t} + \frac{\partial f}{\partial x} + \frac{\partial g}{\partial y} \right] \mathrm{d}t \, \mathrm{d}\Omega^{\mathrm{el}} = 0 \tag{7}$$

As the name indicates, the Taylor–Galerkin finite element model involves Taylor series expansion of the flux term. Inspired by the work of Donea [7], we expand f and g with respect to t and terminate the expansion up to third-order accuracy. To make the scheme more effective in controlling errors, four free parameters α, β, γ, μ are introduced into the series expansion of f and g [16]. The resulting physical fluxes can be expressed as

$$\begin{aligned} f = f^n + \left[\alpha a \frac{\partial \phi}{\partial t} - \beta a \left(\frac{\partial f}{\partial x} + \frac{\partial g}{\partial y} \right) \right] \Bigg|^n (t - t_n) \\ - \frac{1}{2} \left\{ \gamma \left(a^2 \frac{\partial^2 \phi}{\partial t \partial x} + ab \frac{\partial^2 \phi}{\partial t \partial y} \right) - \mu \left[a^2 \left(\frac{\partial^2 f}{\partial x^2} + \frac{\partial^2 g}{\partial x \partial y} \right) \right. \right. \\ \left. \left. + ab \left(\frac{\partial^2 f}{\partial x \partial y} + \frac{\partial^2 g}{\partial y^2} \right) \right] \right\} \Bigg|^n (t - t_n)^2 + \mathcal{O}((t - t_n)^3) \end{aligned} \tag{8}$$

$$g = g^n + \left[\alpha b \frac{\partial \phi}{\partial t} - \beta b \left(\frac{\partial f}{\partial x} + \frac{\partial g}{\partial y}\right)\right]\Bigg|^n (t - t_n)$$
$$-\frac{1}{2}\left\{\gamma\left(ab\frac{\partial^2 \phi}{\partial t \partial x} + b^2 \frac{\partial^2 \phi}{\partial t \partial y}\right) - \mu\left[ab\left(\frac{\partial^2 f}{\partial x^2} + \frac{\partial^2 g}{\partial x \partial y}\right)\right.\right.$$
$$\left.\left.+b^2\left(\frac{\partial^2 f}{\partial x \partial y} + \frac{\partial^2 g}{\partial y^2}\right)\right]\right\}\Bigg|^n (t - t_n)^2 + \mathcal{O}((t - t_n)^3) \tag{9}$$

Note that Equations (8) and (9) are derived at $\alpha + \beta = 1$ and $\gamma + \mu = 1$. In what follows, we specify in this two-dimensional study $\alpha = 0$, $\beta = 1$, $\gamma = 0$ and $\mu = 1$, according to the modified equation analysis, to obtain a third-order spatial accuracy under the smooth flow condition [17].

By approximating $\phi_t = 1/\Delta t(\phi^{n+1} - \phi^n)$ and substituting it, together with Equations (8) and (9), into the weighted residual statement (7), we can derive the consistent-mass finite element equation given below

$$\underline{\underline{\mathbf{M}}}_{\mathrm{c}} \delta \underline{\mathbf{\Phi}}^n = \underline{\mathbf{R}} \tag{10}$$

or

$$\underline{\underline{\mathbf{M}}}_{\mathrm{c}} \underline{\mathbf{\Phi}}^{n+1} = \underline{\mathbf{R}} + \underline{\underline{\mathbf{M}}}_{\mathrm{c}} \underline{\mathbf{\Phi}}^n \tag{11}$$

where $\delta \underline{\mathbf{\Phi}}^n = \underline{\mathbf{\Phi}}^{n-1} - \underline{\mathbf{\Phi}}^n$, $\underline{\mathbf{R}} = \underline{\underline{\mathbf{C}}}\,\underline{\mathbf{f}} + \underline{\underline{\tilde{\mathbf{C}}}}\,\underline{\mathbf{g}} + \underline{\underline{\mathbf{D}}}\,\underline{\mathbf{\Phi}}^n$. In this study, both the weighting function $\mathbf{W}$ and the basis function for $\mathbf{\Phi}$ are chosen to be bi-linear. For additional details about the consistent-mass matrix $\underline{\underline{\mathbf{M}}}_{\mathrm{c}}$ and the residual vector $\underline{\mathbf{R}}$, the reader is referred to Reference [17].

When simulating gas dynamic equations, the employed numerical model should have the ability to resolve shocks and contact discontinuities. No oscillation is permitted to occur near these discontinuities. To achieve this goal, we advance the calculation from t_n to $t_{n+1}(\equiv t_n + \Delta t)$ in two steps. The first step towards enhancing the discrete system is to diagonalize the finite element matrix by lumping $\underline{\underline{\mathbf{M}}}_{\mathrm{c}}$. This lumping-mass approximation, in effect, adds a physically meaningful stabilization term to the equation. The resulting finite element equation is read as

$$\underline{\underline{\mathbf{M}}}_{\mathrm{l}} \underline{\mathbf{\Phi}}^{n+1} = \underline{\mathbf{R}} + \underline{\underline{\mathbf{M}}}_{\mathrm{c}} \underline{\mathbf{\Phi}}^n \tag{12}$$

In the above, $\underline{\underline{\mathbf{M}}}_{\mathrm{l}}$ is the lumping-mass matrix. Adding $-\underline{\underline{\mathbf{M}}}_{\mathrm{l}} \underline{\mathbf{\Phi}}^n$ to both sides of Equation (12), we have

$$\underline{\underline{\mathbf{M}}}_{\mathrm{l}} \delta \underline{\mathbf{\Phi}}^n = \underline{\mathbf{R}} + (\underline{\underline{\mathbf{M}}}_{\mathrm{c}} - \underline{\underline{\mathbf{M}}}_{\mathrm{l}}) \underline{\mathbf{\Phi}}^n \tag{13}$$

Note that the above lumping-mass finite element model is classified as being explicit. The need for expensively solving $\delta \underline{\mathbf{\Phi}}^n$ from a system of algebraic equations in multiple dimensions is, thus, avoided. With these nice features, we, nevertheless, do not regard this explicit model as being computationally excellent since the solution may be excessively smeared by the lumping-mass approximation error. As a simple way to improve prediction accuracy, we introduce the fifth parameter c_{d} and multiply the last term of Equation (13) with it.

The resulting equation reads as

$$\underline{\underline{\mathbf{M}}}_{\mathrm{l}} \delta \underline{\mathbf{\Phi}}^n = \underline{\mathbf{R}} + c_{\mathrm{d}} (\underline{\underline{\mathbf{M}}}_{\mathrm{c}} - \underline{\underline{\mathbf{M}}}_{\mathrm{l}}) \underline{\mathbf{\Phi}}^n \tag{14}$$

Note that the above discrete expression is identical to that proposed by Löhner *et al.* [18]. We, therefore, consider c_d as a diffusion coefficient.

4. MONOTONIC TAYLOR–GALERKIN FINITE ELEMENT MODEL

To provide a theoretical expression for c_d, we need to rewrite Equation (14) as

$$\underline{\underline{\mathbf{M}}}_l \underline{\mathbf{\Phi}}^{n+1} = \underline{\mathbf{Q}}(\underline{\mathbf{\Phi}}^n) + \underline{\underline{\mathbf{M}}}_l \underline{\mathbf{\Phi}}^n \tag{15}$$

where

$$\underline{\mathbf{Q}} = \underline{\mathbf{R}} + c_d(\underline{\underline{\mathbf{M}}}_c - \underline{\underline{\mathbf{M}}}_l)\underline{\mathbf{\Phi}}^n \tag{16}$$

Multiplying Equation (15) by $\underline{\underline{\mathbf{M}}}_l^{-1}$, we have

$$\underline{\mathbf{U}}^{n+1} = \underline{\mathbf{J}}(\underline{\mathbf{\Phi}}^n) \tag{17}$$

where

$$\underline{\mathbf{J}}(\underline{\mathbf{\Phi}}^n) = \underline{\mathbf{\Phi}}^n + \underline{\underline{\mathbf{M}}}_l^{-1}\underline{\mathbf{Q}}(\underline{\mathbf{\Phi}}^n) \tag{18}$$

The vector function $\underline{\mathbf{J}}$ given above accommodates the Gâteaux-derivative property in the interval $[\underline{\mathbf{\Phi}}, \underline{\mathbf{\Phi}}^*]$ [13]. Note that the Jacobian matrix $\underline{\underline{\mathbf{J}}}'(\equiv \partial\underline{\mathbf{J}}/\partial\underline{\mathbf{\Phi}})$ is Riemann integrable and is, thus, derived as

$$\underline{\underline{\mathbf{J}}}' = \underline{\underline{\mathbf{I}}} + \underline{\underline{\mathbf{M}}}_l^{-1}\underline{\underline{\mathbf{Q}}}' \tag{19}$$

or

$$\underline{\underline{\mathbf{J}}}' = \underline{\underline{\mathbf{M}}}_l^{-1}(\underline{\underline{\mathbf{Q}}}' + \underline{\underline{\mathbf{M}}}_l) \tag{20}$$

After some algebra, the discrete equation at (I,J) is derived as

$$\begin{aligned}\delta\underline{\mathbf{\Phi}}_{I,J} = {} & C_{I-1,J+1}\underline{\mathbf{\Phi}}_{I-1,J+1} + C_{I,J+1}\underline{\mathbf{\Phi}}_{I,J+1} + C_{I+1,J+1}\underline{\mathbf{\Phi}}_{I+1,J+1} \\ & + C_{I-1,J}\underline{\mathbf{\Phi}}_{I-1,J} + C_{I,J}\underline{\mathbf{\Phi}}_{I,J} + C_{I+1,J}\underline{\mathbf{\Phi}}_{I+1,J} \\ & + C_{I-1,J-1}\underline{\mathbf{\Phi}}_{I-1,J-1} + C_{I,J-1}\underline{\mathbf{\Phi}}_{I,J-1} + C_{I+1,J-1}\underline{\mathbf{\Phi}}_{I+1,J-1}\end{aligned} \tag{21}$$

where $\delta\underline{\mathbf{\Phi}}_{I,J} = \underline{\mathbf{\Phi}}_{I,J}^{n+1} - \underline{\mathbf{\Phi}}_{I,J}^{n}$ and

$$\begin{aligned}C_{I-1,J+1} = {} & c_d\left(\frac{1}{36} - \frac{1}{24}\alpha v_x + \frac{1}{24}\alpha v_y - \frac{1}{36}\gamma v_x^2 + \frac{1}{12}\gamma v_x v_y - \frac{1}{36}\gamma v_y^2\right) \\ & + \left(\frac{1}{12}v_x - \frac{1}{12}v_y + \frac{1}{12}\beta v_x^2 - \frac{1}{4}\beta v_x v_y + \frac{1}{12}\beta v_y^2\right. \\ & \left. - \frac{1}{6}\mu v_x^2 v_y + \frac{1}{6}\mu v_x v_y^2\right)\end{aligned} \tag{22a}$$

$$C_{I,J+1} = c_{\mathrm{d}} \left(\frac{1}{9} + \frac{1}{6}\,\alpha v_y + \frac{1}{18}\,\gamma v_x^2 - \frac{1}{9}\,\gamma v_y^2 \right) + \left(-\frac{1}{3}\,v_y - \frac{1}{6}\,\beta v_x^2 + \frac{1}{3}\,\beta v_y^2 + \frac{1}{3}\,\mu v_x^2 v_y \right) \tag{22b}$$

$$C_{I+1,J+1} = c_{\mathrm{d}} \left(\frac{1}{36} + \frac{1}{24}\,\alpha v_x + \frac{1}{24}\,\alpha v_y - \frac{1}{36}\,\gamma v_x^2 - \frac{1}{12}\,\gamma v_x v_y - \frac{1}{36}\,\gamma v_y^2 \right) + \left(-\frac{1}{12}\,v_x - \frac{1}{12}\,v_y + \frac{1}{12}\,\beta v_x^2 + \frac{1}{4}\,\beta v_x v_y + \frac{1}{12}\,\beta v_y^2 - \frac{1}{6}\,\mu v_x^2 v_y - \frac{1}{6}\,\mu v_x v_y^2 \right) \tag{22c}$$

$$C_{I-1,J} = c_{\mathrm{d}} \left(\frac{1}{9} - \frac{1}{6}\,\alpha v_x - \frac{1}{9}\,\gamma v_x^2 + \frac{1}{18}\,\gamma v_y^2 \right) + \left(\frac{1}{3}\,v_x + \frac{1}{3}\,\beta v_x^2 - \frac{1}{6}\,\beta v_y^2 - \frac{1}{3}\,\mu v_x v_y^2 \right) \tag{22d}$$

$$C_{I,J} = c_{\mathrm{d}} \left(-\frac{5}{9} + \frac{2}{9}\,\gamma v_x^2 + \frac{2}{9}\,\gamma v_y^2 \right) + \left(-\frac{2}{3}\,\beta v_x^2 - \frac{2}{3}\,\beta v_y^2 \right) \tag{22e}$$

$$C_{I+1,J} = c_{\mathrm{d}} \left(\frac{1}{9} + \frac{1}{6}\,\alpha v_x - \frac{1}{9}\,\gamma v_x^2 + \frac{1}{18}\,\gamma v_y^2 \right) + \left(-\frac{1}{3}\,v_x + \frac{1}{3}\,\beta v_x^2 - \frac{1}{6}\,\beta v_y^2 + \frac{1}{3}\mu v_x v_y^2 \right) \tag{22f}$$

$$C_{I-1,J-1} = c_{\mathrm{d}} \left(\frac{1}{36} - \frac{1}{24}\,\alpha v_x - \frac{1}{24}\,\alpha v_y - \frac{1}{36}\,\gamma v_x^2 - \frac{1}{12}\,\gamma v_x v_y - \frac{1}{36}\,\gamma v_y^2 \right) + \left(\frac{1}{12}\,v_x + \frac{1}{12}\,v_y + \frac{1}{12}\,\beta v_x^2 + \frac{1}{4}\,\beta v_x v_y + \frac{1}{12}\,\beta v_y^2 + \frac{1}{6}\,\mu v_x^2 v_y + \frac{1}{6}\,\mu v_x v_y^2 \right) \tag{22g}$$

$$C_{I,J-1} = c_{\mathrm{d}} \left(\frac{1}{9} - \frac{1}{6}\,\alpha v_y + \frac{1}{18}\,\gamma v_x^2 - \frac{1}{9}\,\gamma v_y^2 \right) + \left(\frac{1}{3}\,v_y - \frac{1}{6}\,\beta v_x^2 + \frac{1}{3}\,\beta v_y^2 - \frac{1}{3}\,\mu v_x^2 v_y \right) \tag{22h}$$

$$C_{I+1,J-1} = c_{\mathrm{d}} \left(\frac{1}{36} + \frac{1}{24}\alpha v_x - \frac{1}{24}\alpha v_y - \frac{1}{36}\gamma v_x^2 + \frac{1}{12}\gamma v_x v_y - \frac{1}{36}\gamma v_y^2 \right)$$
$$+ \left(-\frac{1}{12} v_x + \frac{1}{12} v_y + \frac{1}{12}\beta v_x^2 - \frac{1}{4}\beta v_x v_y + \frac{1}{12}\beta v_y^2 \right.$$
$$\left. + \frac{1}{6}\mu v_x^2 v_y - \frac{1}{6}\mu v_x v_y^2 \right) \tag{22i}$$

In the above, $v_x (\equiv a\Delta t/\Delta x)$ and $v_y (\equiv b\Delta t/\Delta y)$ are known as the Courant numbers.

The explicit scheme given in (17) is, by definition, monotonic. This implies that if $\underline{\mathbf{\Phi}} - \underline{\mathbf{\Phi}}^* \geqslant 0$, then $\underline{\mathbf{J}}(\underline{\mathbf{\Phi}}) - \underline{\mathbf{J}}(\underline{\mathbf{\Phi}}^*) \geqslant 0$. Given the Gâteaux-derivative function $\underline{\mathbf{J}}$ and the Riemann integral function $\underline{\underline{\mathbf{J}}}'$, the mean-value theorem is applied to derive

$$\underline{\mathbf{J}}(\underline{\mathbf{\Phi}}) - \underline{\mathbf{J}}(\underline{\mathbf{\Phi}}^*) = (\underline{\mathbf{\Phi}} - \underline{\mathbf{\Phi}}^*) \int_{-1}^{0} [\underline{\underline{\mathbf{J}}}'(\underline{\mathbf{\Phi}} + t(\underline{\mathbf{\Phi}} - \underline{\mathbf{\Phi}}^*))] \, \mathrm{d}t \tag{23}$$

Assume that $\underline{\mathbf{\Phi}} - \underline{\mathbf{\Phi}}^* \geqslant 0$ and $\underline{\underline{\mathbf{J}}}'(\bar{\underline{\mathbf{\Phi}}}) \geqslant 0$ for $\bar{\mathbf{\Phi}}$ belonging to the open interval of $\underline{\mathbf{\Phi}}$ and $\underline{\mathbf{\Phi}}^*$; then, $\underline{\mathbf{J}}(\underline{\mathbf{\Phi}}) - \underline{\mathbf{J}}(\underline{\mathbf{\Phi}}^*) \geqslant 0$. As a result, the developed explicit Taylor–Galerkin model is monotonic in time provided that $\underline{\underline{\mathbf{J}}}'(\underline{\mathbf{\Phi}})$ is monotonic. This enables us to determine c_{d} by demanding that $\underline{\underline{\mathbf{I}}} + \underline{\underline{\mathbf{M}}}_{\mathrm{l}}^{-1} \underline{\underline{\mathbf{Q}}}'$ be monotonic. More precisely, the developed explicit model is monotonic in time if $\underline{\underline{\mathbf{I}}} + \underline{\underline{\mathbf{M}}}_{\mathrm{l}}^{-1} \underline{\underline{\mathbf{Q}}}'$ is a monotone matrix. A possible way to make $\underline{\underline{\mathbf{I}}} + \underline{\underline{\mathbf{M}}}_{\mathrm{l}}^{-1} \underline{\underline{\mathbf{Q}}}'$ monotonic is to require that $\underline{\underline{\mathbf{M}}}_{\mathrm{l}}$ be an M-matrix, and that the Jacobian of $\underline{\mathbf{Q}}$ given in Equation (16) be non-negative.

By virtue of the above M-matrix theory, the task of expressing c_{d} in terms of v_x and v_y is now transformed into that of finding c_{d} from the following inequalities:

$$c_{\mathrm{d}} + 3v_x - 3v_y + 3v_x^2 - 9v_x v_y + 3v_y^2 - 6v_x^2 v_y + 6v_x v_y^2 \geqslant 0 \tag{24a}$$
$$2c_{\mathrm{d}} - 6v_y - 3v_x^2 + 6v_y^2 + 6v_x^2 v_y \geqslant 0 \tag{24b}$$
$$c_{\mathrm{d}} - 3v_x - 3v_y + 3v_x^2 + 9v_x v_y + 3v_y^2 - 6v_x^2 v_y - 6v_x v_y^2 \geqslant 0 \tag{24c}$$
$$2c_{\mathrm{d}} + 6v_x + 6v_x^2 - 3v_y^2 - 6v_x v_y^2 \geqslant 0 \tag{24d}$$
$$5c_{\mathrm{d}} + 6(v_x^2 + v_y^2) \geqslant 0 \tag{24e}$$
$$2c_{\mathrm{d}} - 6v_x + 6v_x^2 - 3v_y^2 + 6v_x v_y^2 \geqslant 0 \tag{24f}$$
$$c_{\mathrm{d}} + 3v_x + 3v_y + 3v_x^2 + 9v_x v_y + 3v_y^2 + 6v_x^2 v_y + 6v_x v_y^2 \geqslant 0 \tag{24g}$$
$$2c_{\mathrm{d}} + 6v_y - 3v_x^2 + 6v_y^2 - 6v_x^2 v_y \geqslant 0 \tag{24h}$$
$$c_{\mathrm{d}} - 3v_x + 3v_y + 3v_x^2 - 9v_x v_y + 3v_y^2 + 6v_x^2 v_y - 6v_x v_y^2 \geqslant 0 \tag{24i}$$

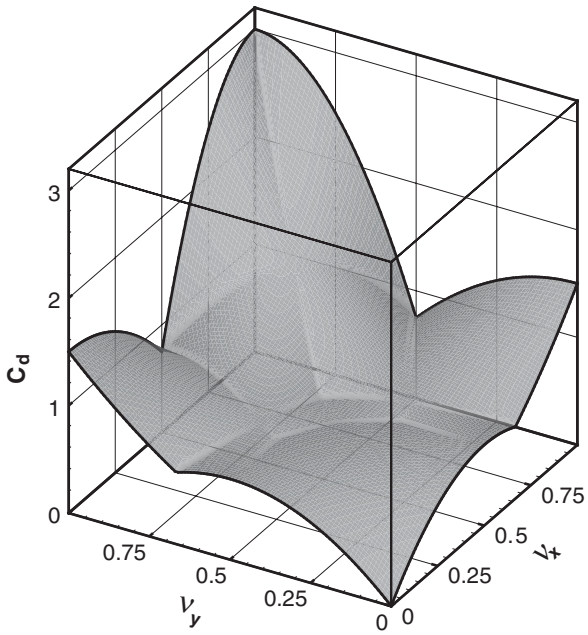

Figure 1. The range of c_d, plotted against the Courant numbers v_x and v_y, for the chosen free parameters at $\alpha = 0$, $\beta = 1$, $\gamma = 0$ and $\mu = 1$.

Note that the above equations are obtained at $\alpha = 0$, $\beta = 1$, $\gamma = 0$ and $\mu = 1$. In addition, $c_d(v_x, v_y)$ is chosen to lie slightly above the surface plotted in Figure 1 so as to render satisfaction of Equation (24). Under the circumstances, the monotonicity-preserving feature is retained. It is stressed that the above theoretically derived two-dimensional finite element model involves no complex spatial operator splitting.

5. FUNDAMENTAL STUDY OF THE FINITE ELEMENT MODEL

We now conduct modified equation analysis [19] to reveal how dissipation and dispersion errors can be reduced with the increasingly smaller grid sizes Δx and Δy. By performing Taylor series expansion on terms given in Equation (21), we can derive the modified equation as follows for the discretization equation obtained at $\alpha = 0$, $\beta = 1$, $\gamma = 0$ and $\mu = 1$:

$$\begin{aligned}
&\phi_t + a\phi_x + b\phi_y \\
&\quad = \frac{1}{6} c_d \frac{\Delta x^2}{\Delta t} \phi_{xx} + \frac{1}{6} c_d \frac{\Delta y^2}{\Delta t} \phi_{yy} \\
&\qquad + \frac{1}{6}(-1 + c_d + v_x^2) v_x \frac{\Delta x^3}{\Delta t} \phi_{xxx} + \frac{1}{6}(-1 + c_d + v_y^2) v_y \frac{\Delta y^3}{\Delta t} \phi_{yyy}
\end{aligned}$$

$$+\frac{1}{6}(-1+c_{\mathrm{d}}+v_x^2)v_y\frac{\Delta x^2\Delta y}{\Delta t}\phi_{xxy}+\frac{1}{6}(-1+c_{\mathrm{d}}+v_y^2)v_x\frac{\Delta x\Delta y^2}{\Delta t}\phi_{xyy}$$

$$-\frac{1}{72}(-c_{\mathrm{d}}+c_{\mathrm{d}}^2-6c_{\mathrm{d}}v_x^2+9v_x^2-9v_x^4)\frac{\Delta x^4}{\Delta t}\phi_{xxxx}$$

$$-\frac{1}{72}(-c_{\mathrm{d}}+c_{\mathrm{d}}^2-6c_{\mathrm{d}}v_y^2+9v_y^2-9v_y^4)\frac{\Delta y^4}{\Delta t}\phi_{yyyy}$$

$$+\frac{1}{6}(-1+c_{\mathrm{d}}+v_x^2)v_xv_y\frac{\Delta x^3\Delta y}{\Delta t}\phi_{xxxy}+\frac{1}{6}(-1+c_{\mathrm{d}}+v_y^2)v_xv_y\frac{\Delta x\Delta y^3}{\Delta t}\phi_{xyyy}$$

$$+\frac{1}{36}(c_{\mathrm{d}}-c_{\mathrm{d}}^2+3c_{\mathrm{d}}(v_x^2+v_y^2)-3(v_x^2+v_y^2)+3v_x^2v_y^2)\frac{\Delta x^2\Delta y^2}{\Delta t}\phi_{xxyy}+\cdots \tag{25}$$

The derived modified equation for (6) confirms the consistency-preserving property and reveals the temporal and spatial error distributions.

We then conduct phase response analysis to compute the ratio of the semi-discrete phase velocity $\mathbf{C}_{\mathrm{TG}}$ to the exact phase velocity $\mathbf{C}_{\mathrm{exact}}$:

$$r_\Phi=\frac{\mathbf{C}_{\mathrm{TG}}}{\mathbf{C}_{\mathrm{exact}}} \tag{26}$$

For the two-dimensional equation (6), the exact phase velocity (or frequency), namely, $\mathbf{C}_{\mathrm{exact}}=-\Delta t((a,b)\cdot(q_x,q_y))$, is easily derived as

$$\Phi_{\mathrm{exact}}=\Phi_0\mathrm{e}^{\mathrm{i}(q_x(x-at)+q_y(y-bt))} \tag{27}$$

where q_x and q_y denote the wave numbers along the x and y directions, respectively. In the case of $\Delta x=\Delta y=h$, we can normalize the dimensional wave number vector $\vec{\xi}$ by

$$\vec{\xi}=(\xi,\eta)=(hq_x,hq_y) \tag{28}$$

We rewrite the velocity vector in terms of the flow direction $\theta\equiv\tan^{-1}(b/a)$, where

$$(a,b)=(a^2+b^2)^{1/2}(\cos\theta,\sin\theta) \tag{29}$$

According to the von Neumann stability analysis (or Fourier analysis) [20], the amplification factor G and phase velocity $\mathbf{C}_{\mathrm{TG}}$ for the discrete equation (21) are derived as

$$G=V_1+\mathrm{i}V_2=\text{function }(|\xi|,\theta) \tag{30}$$

$$\mathbf{C}_{\mathrm{TG}}=\tan^{-1}\left(\frac{V_2}{V_1}\right) \tag{31}$$

where

$$V_1=1-\tfrac{5}{9}c_{\mathrm{d}}+\tfrac{2}{9}c_{\mathrm{d}}(\cos(\xi)+\cos(\eta))-\tfrac{2}{3}(v_x^2+v_y^2)$$

$$+\tfrac{1}{3}v_x^2(2\cos(\xi)-\cos(\eta))+\tfrac{1}{3}v_y^2(2\cos(\eta)-\cos(\xi))$$

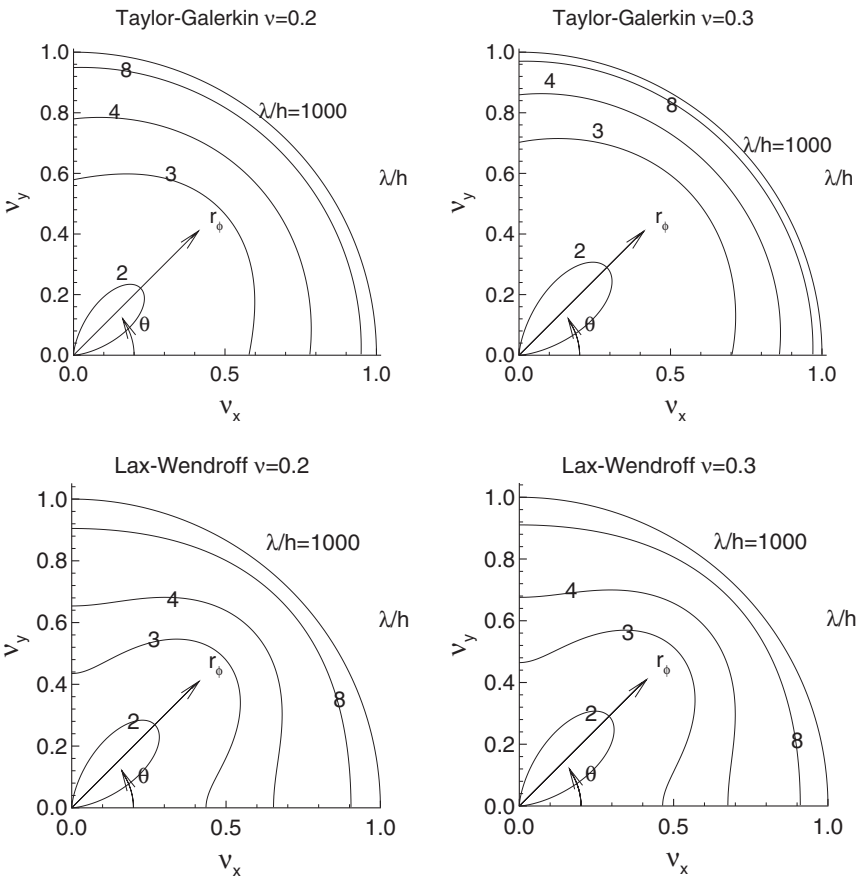

Figure 2. The relative phase error r_Φ, defined in (26), for the proposed Taylor–Galerkin method and Lax–Wendroff method.

$$+\tfrac{1}{18}\,c_{\mathrm{d}}(\cos(\xi+\eta)+\cos(\xi-\eta))+\tfrac{1}{6}\,v_x^2(\cos(\xi+\eta)+\cos(\xi-\eta))$$

$$+\tfrac{1}{2}\,v_x v_y(\cos(\xi+\eta)-\cos(\xi-\eta))+\tfrac{1}{6}\,v_y^2(\cos(\xi+\eta)+\cos(\xi-\eta)) \tag{32}$$

$$V_2=-\tfrac{2}{3}\,(v_x\sin(\xi)+v_y\sin(\eta))+\tfrac{2}{3}\,v_x v_y(v_y\sin(\xi)+v_x\sin(\eta))$$

$$-\tfrac{1}{6}\,v_x(\sin(\xi+\eta)+\sin(\xi-\eta))-\tfrac{1}{6}\,v_y(\sin(\xi+\eta)-\sin(\xi-\eta))$$

$$-\tfrac{1}{3}\,v_x^2 v_y(\sin(\xi+\eta)-\sin(\xi-\eta))-\tfrac{1}{3}\,v_x v_y^2(\sin(\xi+\eta)+\sin(\xi-\eta)) \tag{33}$$

The above phase response analysis clearly shows that the value of r_Φ, defined in Equation (26), depends on the wavelength λ $(=2\pi h/|\xi|)$ and the angle θ. Noticeably seen from Figure 2, which plots r_Φ at different wavelengths, is the significantly improved isotropy even at a small wavelength.

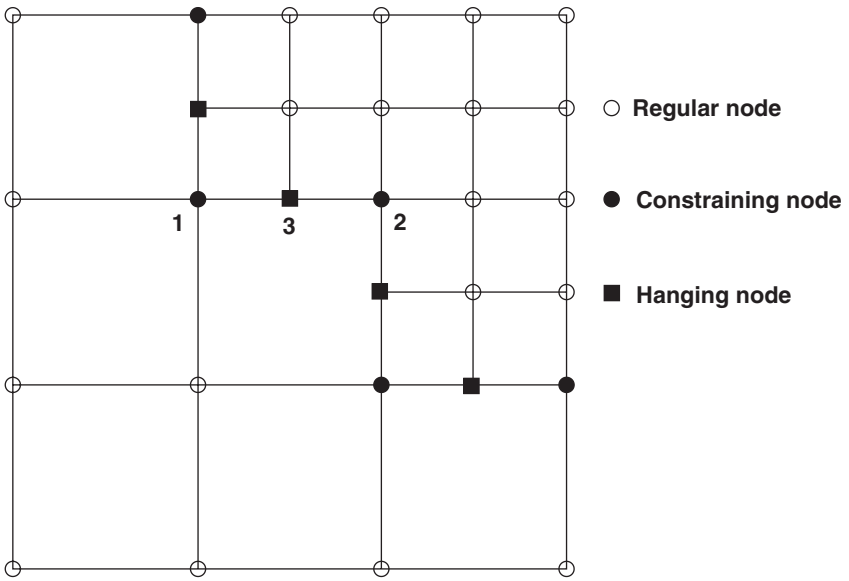

Figure 3. The illustration of hanging nodes.

6. *h*-ADAPTIVE MONOTONIC FINITE ELEMENT MODEL

A sharp capture of thermodynamic variables in gas dynamic system calls for a high-resolution discontinuity-capturing model. To make the developed monotone finite element model computationally more efficient and useful in practice, we will further refine the Taylor–Galerkin model given previously in Sections 3 and 4 by incorporating the grid-adaptive ability into the formulation. In this paper, the *h*-adaptive method is chosen to refine solutions in high-gradient regions, thus improving the overall prediction quality at reasonable cost. Success in grid refinement depends on, among other factors, complications in the data structure, bookkeeping of remeshed nodes, and the treatment of constrained nodes [21].

Within the finite element framework, solutions at the irregular nodes (or hanging nodes) are not directly obtained from the finite element matrix equation. Rather, they are algebraically averaged from the neighbouring solutions obtained at regular nodes (or nodes shared by all neighbouring elements), which lie on the constraining side. For example, ϕ_3 at the hanging node 3 in Figure 3 is constrained by $\phi_3 = \frac{1}{2}(\phi_1 + \phi_2)$. In the presence of irregular nodes, the global mass matrix is modified to improve the overall efficiency [14]. The rule adopted to make modification on the global mass matrix has been detailed in Reference [22].

7. NUMERICAL RESULTS

The proposed Taylor–Galerkin finite element model will be validated against several benchmark tests. We considered firstly the Sod's problem [23], subject to the initial data

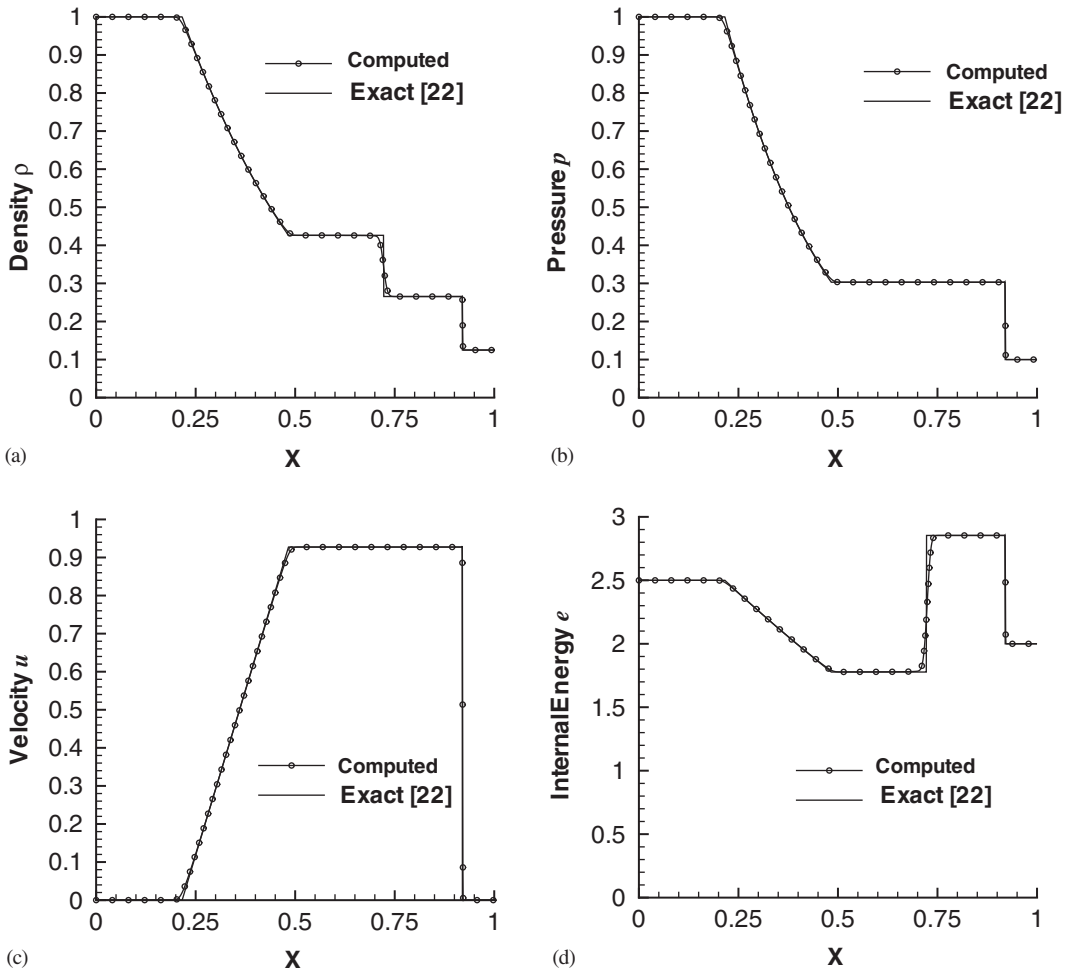

Figure 4. The simulated shock-tube solutions at $t = 0.24$. (a) Density; (b) pressure; (c) velocity; (d) internal energy.

given by

$$(\rho, u, p) = \begin{cases} (1, 0, 1), & 0 \leqslant x \leqslant 0.5 \\ (0.125, 0, 0.1), & 0.5 < x \leqslant 1 \end{cases} \tag{34}$$

For this analytic problem, the finite element solution was sought at $v_x = 0.85$ and $v_y = 0$. The value of c_d is theoretically specified according to Equations (24). Figure 4 compares the simulated solution (symbol) with the exact solution (full line) [23]. The developed Taylor–Galerkin model is seen to be able to resolve shock discontinuities within few grid points. The contact discontinuities are, unfortunately, smeared with more mesh points. There are no overshoots or undershoots.

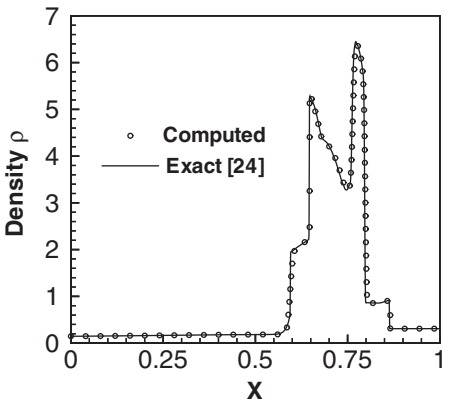

Figure 5. The simulated density is plotted against x for the blasting wave problem.

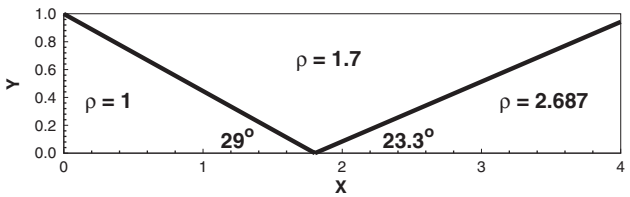

Figure 6. Schematic of the shock reflection problem.

The blasting wave problem [24], subject to the following initial data, is then investigated:

$$(\rho, u, p) = \begin{cases} (1, 0, 1000), & 0 \leqslant x \leqslant 0.1 \\ (1, 0, 0.1), & 0.1 < x \leqslant 0.9 \\ (1, 0, 100), & 0.9 < x \leqslant 1.0 \end{cases} \tag{35}$$

This problem was solved at $v = 0.85$ in a uniformly discretized domain. Since this problem is not amenable to an exact solution, the TVB solution given in Reference [25] is considered as the referenced solution. The results (symbols) plotted in Figure 5 show that the proposed finite element model can reproduce the known wave propagation feature.

Having validated the ability of the proposed model to capture shock and contact discontinuities in a domain of single dimension, we proceed to solve for the two-dimensional benchmark tests at $\alpha = 0$, $\beta = 1$, $\gamma = 0$ and $\mu = 1$. As before, the value of c_d was prescribed according to Equation (24). The first two-dimensional validation test considers the shock reflection from a flat plate [26]. In Figure 6, an oblique shock wave having a Mach number of 2.9 is seen to reflect from the channel floor at an angle of 29° to the incident flow. The physical domain was uniformly discretized from the beginning of the simulation. It is seen from Figure 7 that grids are adaptively concentrated along the track of shock impingement and its reflection. The simulated results (symbols) in Figure 8 agree well with the exact solutions (full line)

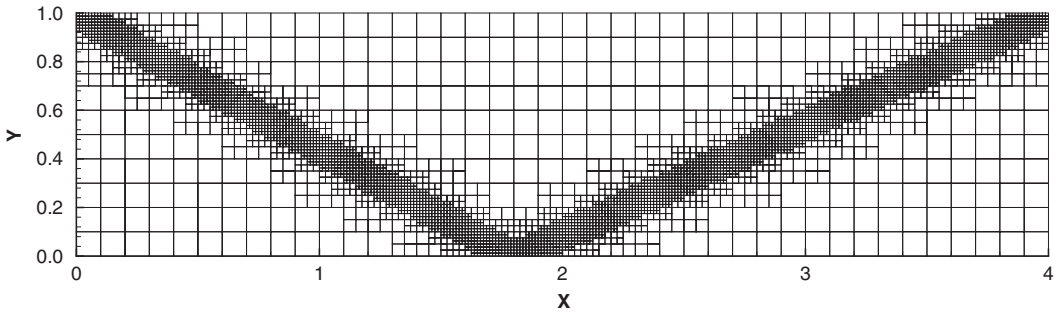

Figure 7. The adaptive meshes generated in the simulation of shock reflection problem.

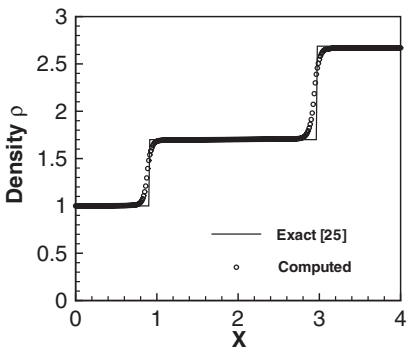

Figure 8. A comparison of the simulated and exact solutions for density along the line $y = 0.5$.

[26]. Through this test, the proposed two-dimensional hyperbolic model is confirmed to be able to provide ripple-free positive-valued solutions without requiring excessive mesh points to resolve shocks. The model may, therefore, be computationally less expensive to obtain the two-dimensional gas dynamic solutions.

We then consider the wind tunnel problem of Woodward and Colella [24]. This problem has been investigated by many authors to study the time-evolving contact discontinuities and regular shocks. As the Mach reflection is seen to emanate from the channel wall, a slip line is, thus, expected to occur at the junction of the Mach shock and the reflected shock. The tunnel in Figure 9 has a length 3, a width 1 and a step, which is 0.2 in height and is located downstream of the channel inlet with a length of 0.6. The entry flow is uniform in velocity with the Mach number of 3. At the channel exit, all field variables are assumed to be gradient-free and, thus, have no effect on the flow development. At the channel roof, we specify the reflecting boundary condition: $\partial u/\partial x = 0$, $v = 0$. Along the channel floor and step, we simply apply the slip condition. No flow is allowed to penetrate the channel wall. At the step corner, the rarefraction fan is seen to occur and this corner is, in fact, a sonic point. Like many other studies, no specific treatment is needed at this geometrically and physically singular corner. The implication of this simplification is that the discretization error may cause

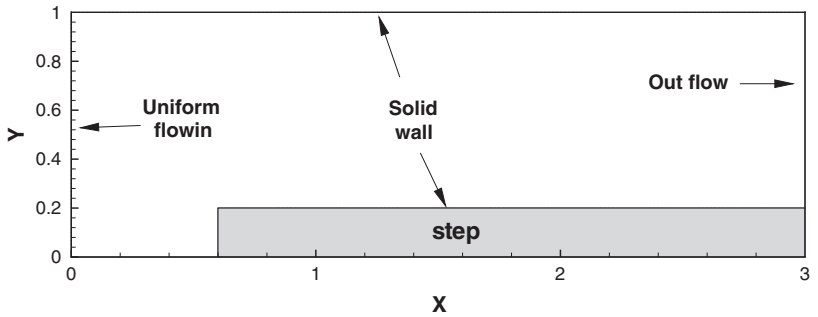

Figure 9. Schematic of the flow in a channel having a step.

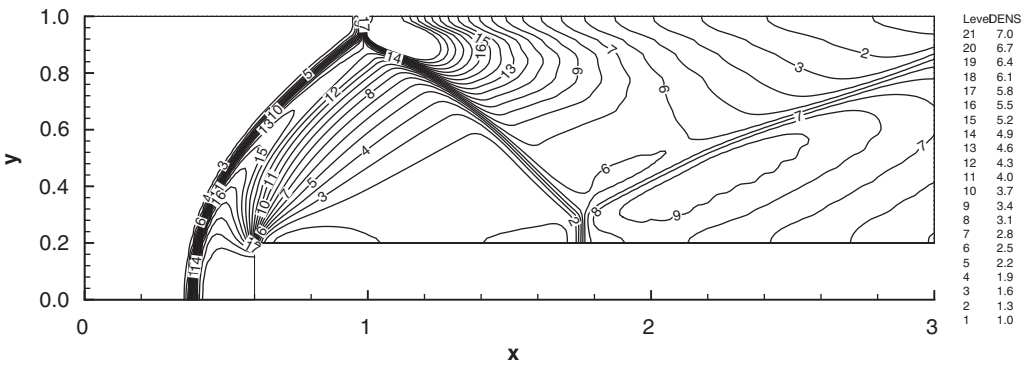

Figure 10. The simulated density contours.

an artificial boundary layer to develop along the planar step and, in turn, contaminate the prediction.

Numerical solutions obtained at $\Delta x = \Delta y = 1/60$ are shown in Figure 10. Due to space limitation, only the density contours are plotted at $t = 3.0$. Ahead of the step, the simulated shock bends towards the primary flow direction and interacts with the expansion waves stemming from the step corner. The oblique shock impinges on the channel roof, resulting in a Mach shock wave that is locally orthogonal to the channel roof. Such a reflection differs from the regular reflection and is, thus, called Mach reflection. It is remarkable to see from Figure 10 the slip line, which originates from the junction of the incident shock, Mach shock, and reflected shock waves. This slip line is physically identical to the contact discontinuity. As a consequence, the flow properties are not expected to be continuous across the slip line. Figure 10 also shows the reflected oblique shock from the channel roof, followed by a reflection from the channel floor. The Mach stem on the step has a length longer than that on the channel wall. This finding is similar to that found previously by Chang *et al.* [27].

8. CONCLUDING REMARKS

In this paper we develop a Taylor–Galerkin finite element model to simulate Euler equations for gas dynamics. To improve the computational efficiency, the finite element equation has been developed within the explicit context. To minimize the artificial diffusion error, the diffusion coefficient has been rigorously determined to exhibit the monotonicity-preserving and strictly positive-valued density properties based on the M-matrix theory. To improve the prediction accuracy, the h-adaptive capability is introduced into the formulation so that sharp profiles can be obtained in a domain discretized by a much reduced number of grid points. Several cases have been studied to demonstrate the stability, accuracy, and efficiency of the developed finite element model. These problems involve shocks and contact discontinuities and are, thus, appropriate for justifying the usefulness of the proposed model for simulating gas dynamic equations. All the simulated results have been shown to be in good agreement with the reliable comparison data.

ACKNOWLEDGEMENTS

This work was supported by the National Science Council of the Republic of China, Grant NSC 88-2611-E-002-025. The facility provided by Professor K. Morgan in the course of the first author's 1-year stay in Swansea is also appreciated.

REFERENCES

1. Morton KW. Generalized Galerkin methods for hyperbolic problems. *Computer Methods in Applied Mechanics and Engineering* 1985; **52**:847–871.
2. Lesaint P, Raviart PA. On a finite element method for solving the neutron transport problems. In *Mathematical Aspects of Finite Elements in Partial Differential Equations*, de Boor C (ed.). Academic Press: New York, 1974; 89–123.
3. Lee JHW, Peraire J, Zienkiewicz OC. The characteristic Galerkin method for advection dominated problems—an assessment. *Computer Methods in Applied Mechanics and Engineering* 1987; **61**:359–369.
4. Donea J. Generalized Galerkin methods for convection dominated transport phenomena. *Applied Mechanics Review* 1991; **44**:205–214.
5. Hughes TJR, Mallet M, Mizukami A. A new finite element formulation for computational fluid dynamics: II. Beyond SUPG. *Computer Methods in Applied Mechanics and Engineering* 1986; **54**:341–355.
6. Christie I, Griffiths DF, Mitchell AR, Zienkiewicz OC. Finite element methods for second order differential equations with significant first derivatives. *International Journal for Numerical Methods in Engineering* 1976; **10**:1389–1396.
7. Donea J. A Taylor–Galerkin method for convective transport problems. *International Journal for Numerical Methods in Engineering* 1984; **20**:101–119.
8. LeVeque RJ. *Numerical Methods for Conservation Laws* (2nd edn). Birkhäuser: Basel, 1992.
9. Harten A. High-resolution schemes for hyperbolic conservation laws. *Journal of Computational Physics* 1983; **49**:357–393.
10. Meis T, Marcowitz U. *Numerical Solution of Partial Differential Equations*, *Applied Mathematical Sciences*, vol. 32. Springer: New York, 1981.
11. Ikeda T. *Maximal Principle in Finite Element Models for Convection–Diffusion Phenomena*, *Lecture Notes in Numerical and Applied Analysis*, vol. 4. Kinokuniya Company Ltd.: Tokyo, Japan, 1983.
12. Ahués M, Telias M. Petrov–Galerkin Scheme for the steady state convection diffusion equation. In *Fourth Int. Conf. on Finite Elements in Water Resources*, Holz KP, Meissner U, Zielbe W, Brebbia CA, Pendier G, Gray W (eds). Springer Verlag: Southampton, pp. 2–3, 2–12, 1982.
13. Øistein Bøe. A monotone Petrov–Galerkin method for quasilinear parabolic differential equations. *SIAM Journal of Scientific Computing* 1993; **14**:1057–1071.
14. Demkowicz L, Oden JT, Rachowicz W, Hardy O. Toward a universal h-p adaptive finite element strategy, Part I: Constrained approximation and data structure. *Computer Methods in Applied Mechanics and Engineering* 1989; **77**:79–112.

15. Lax PD. Hyperbolic systems of conservation laws, II. *Communications on Pure and Applied Mathematics* 1957; **10**:537–566.
16. Sheu TWH, Fang CC. A numerical study of nonlinear propagation of disturbances in two-dimensions. *Journal of Computational Acoustics* 1996; **4**:291–319.
17. Fang CC. Development of a finite element method for inviscid Euler equations. *Ph.D. Thesis*, Department of Naval Architecture and Ocean Engineering, National Taiwan University, April 2000.
18. Löhner R, Morgan K, Peraire J, Vahdati M. Finite element flux-corrected transport (FEM-FCT) for the Euler and Navier–Stokes equations. *International Journal for Numerical Methods in Fluids* 1987; **7**:1093–1109.
19. Warming RF, Hyett BJ. The modified equation approach to the stability and accuracy analysis of finite-difference methods. *Journal of Computational Physics* 1974; **14**:159–179.
20. ÓBrien GG, Hyman MA, Kaplan S. A study of the numerical solution of partial differential equations. *Journal of Mathematical Physics* 1950; **29**:223–251.
21. Demkowicz L, Oden JT. A review of local refinement techniques and the corresponding data structure in *h*-type adaptive finite element methods. *TICOM Report 88-02*, The Texas Institute for Computational Mechanics, The University of Texas at Austin, TX 78712, 1988.
22. Sheu TWH, Fang CC, Tsai SF, Hwang CY. On an adaptive monotonic convection–diffusion flux discretization scheme. *Computer Methods in Applied Mechanics and Engineering* 1999; **173**(1–2):201–215.
23. Sod G. A survey of several finite difference methods for system of nonlinear hyperbolic conservation laws. *Journal of Computational Physics* 1978; **27**:1–31.
24. Woodward P, Colella P. The numerical simulation of two-dimensional fluid flow with strong waves. *Journal of Computational Physics* 1984; **54**:115–173.
25. Cockburn B, Lin SY, Shu CW. TVB Runge–Kutta local projection discontinuous Galerkin finite element method for conservation laws, III: one-dimensional systems. *Journal of Computational Physics* 1989; **84**:90–113.
26. Yee HC, Warming RF, Harten A. Implicit total variation diminishing (TVD) schemes for steady state calculations. *Journal of Computational Physics* 1985; **57**:327–360.
27. Chang SC, Wang XY, Chow CY. The space–time conservation element and solution element method: a new high-resolution and genuinely multidimensional paradigm for solving conservation laws. *Journal of Computational Physics* 1999; **156**:89–136.

